Mulder, J.A., et al., 2019, A Multiproxy provenance approach to uncovering the assembly of East Gondwana in Antarctica: Geology, https://doi.org/10.1130/G45952.1

Appendix DR1: Feldspar Pb isotope method by laser ablation quadrupole inductively coupled mass spectrometry

The Pb isotopes of feldspars were measured by a quadrupole inductively coupled mass spectrometer and sampled using an excimer laser (LA-ICPMS). Although quadrupole mass spectrometers are not as precise as multi-collector instruments, they are more versatile in allowing rapid measurement of Pb over a wide range of concentrations and the ability to monitor a wide range of masses during ablation. Monitoring masses that potentially interfere with the analysis such as Hg, U, and Th is important for laser-based analysis, as the laser often encounters subsurface inclusions that can produce inaccurate results. Laser quadrupole-based mass spectrometer Pb isotope measurements have been used extensively at the University of Tasmania to provide accurate measurements on sulphides, phosphates, oxides and silicates including feldspars (e.g., Davidson et al., 2007; Meffre et al., 2008; Woodhead et al., 2009; Large et al., 2013; Lai et al., 2014, Doyle et al., 2015; Hawke et al., 2015). Other laboratories are also using quadruple instruments to measure Pb isotopes in feldspars (e.g., Wohlgemuth-Ueberwasser et al., 2017).

Pb-isotopes and trace elements were measured in 6 analytical sessions between 24 May 2016 and 6 March 2017 using a quadrupole LA-ICPMS housed at the University of Tasmania. An ASI RESOlution S155 laser ablation system utilizing a Coherent Compex Pro 110 ArF excimer laser operating at 193nm wavelength and a 20ns pulse width was coupled to an Agilent 7900 quadrupole ICPMS for all Pb isotopic measurements. Ablation was carried out in a He atmosphere flowing at 0.35 l/min and mixed with Ar immediately after the ablation. Precision on the Pb isotopic ratios was improved from the standard LA-ICPMS setup as follows:

- A smoothing manifold (squid Müller et al., 2009) was used to minimize laser shot noise and issues related to the sequential isotope acquisition on the quadrupole
- A particle-separator (Guillong et al., 2003) was used between the laser and the plasma torch to trap particles and minimize spikes in the mass spectrometer signals
- 110µm lines (moving at 5 μms^{-1}) were used rather than spots to minimize signal decrease that is present in spot analysis.
- A moderate fluence (3.5 J/cm^2) was used to ensure efficient ablation and to minimize spikes but without causing melting or extensive deposition around the ablation site.
- Pure silica glass was ablated between samples and standards to remove particles from the tubing and from the ablation cell, ensuring fewer spikes and decreasing inter sample contamination.
- The ^{202}Hg to ^{204}Hg mass bias was determined from the background gas measurement and used for accurate Hg isobaric interference correction on ^{204}Pb. Background Hg varied between 400 and 1400 counts per second depending on the analytical run.
- Gold traps were used on the gas lines to remove Hg from the Ar and He gasses. The daily ablation cell glass was cleaned prior to each laser ablation run to remove Pb, Hg, and other potential contaminants.
- The results of each analysis were examined carefully and ratios where the detector switched from the pulse to analogue modes during an analysis were filtered and not used for the final data compilation (approximately 3—4 million counts per second depending on the analytical run and the isotope measured).

The main parameters used in the analyses are listed in the table below. Data processing was undertaken using in-house Excel-based spreadsheets. The ratios were calculated using 2 spots on the primary standards (NIST610) with groups of standards bracketing each group of unknowns (30—40 analyses). Very little instrumental drift was observed in each of the analytical runs on the isotope ratios (typically <0.2% in 6—8 hours of analysis). Each group of standards included 2 spots or lines on check standards (BCR-2g and GSD-1g) and 2 spots on a pure silica glass. All Pb isotope ratios for BCR-2g and GSD-1g where within the recommended values (http://georem.mpch-mainz.gwdg.de) when both the uncertainty on the analytical runs and the uncertainty on recommended ratios are considered. Feldspars Pb isotopes standards were not available in 2016—2017 when these samples were analysed, however Pb isotopic studies on sulphides (e.g., Woodhead et al., 2009), zircons (e.g., Meffre et al., 2008) and phosphates (e.g., Cherry et al., 2018) show that there are no laser-induced matrix effects on the Pb isotopes ratios between sulphides, silicates, and the calibration glasses (e.g., the NIST glasses) as long as the pulse to analogue transition is not crossed and the Hg correction is calculated correctly. This lack of matrix effect has been confirmed for K-feldspars in 2018 during the development of an in-house K-feldspar standard analysed both on the LA-ICPMS and by isotope dilution multi-collector ICPMS (Chapman et al., *in review*).

Although Na, Mg, Al, Si, P, K, Ca, Ti, Fe, and Ba data was collected and used to recognize parts of the feldspars that were free of inclusions and therefore suitable for Pb isotopic analysis (e.g., Appendix DR1 Fig. 1), the trace element data was not converted to concentrations. The results would not have been directly relevant to this study but could be used for future studies to inform on magmatic and metamorphic processes. However, all the background corrected count rates have been reported in the data spreadsheet.

References

Cherry, A. R., Kamenetsky, V. S., McPhie, J., Thompson, J. M., Ehrig, K., Meffre, S., Kamenetsky, M. B., and Krneta, S., 2018, Tectonothermal events in the Olympic IOCG Province constrained by apatite and REE-phosphate geochronology: Australian Journal of Earth Sciences, v. 65, no. 5, p. 643-659.

Davidson, G. J., Paterson, H., Meffre, S., and Berry, R. F., 2007, Characteristics and origin of the oak dam East Breccia-Hosted, iron oxide Cu-U-(Au) Deposit: Olympic Dam region, Gawler Craton, South Australia: Economic Geology, v. 102, no. 8, p. 1471-1498.

Doyle, M. G., Fletcher, I. R., Foster, J., Large, R. R., Mathur, R., McNaughton, N. J., Meffre, S., Muhling, J. R., Phillips, D., and Rasmussen, B., 2015, Geochronological constraints on the Tropicana gold deposit and Albany-Fraser orogen, Western Australia: Economic Geology, v. 110, no. 2, p. 355-386.

Guillong, M., Kuhn, H. R. & Günther, D. 2003. Application of a particle separation device to reduce inductively coupled plasma-enhanced elemental fractionation in laser ablation-inductively coupled plasma-mass spectrometry. Spectrochimica Acta - Part B Atomic Spectroscopy, v. 58, 211-220.

Hawke, M. L., Meffre, S., Stein, H., Hilliard, P., Large, R., and Gemmell, J. B., 2015, Geochronology of the DeGrussa volcanic-hosted massive sulphide deposit and associated mineralisation of the Yerrida, Bryah and Padbury Basins, Western Australia: Precambrian Research, v. 267, p. 250-284.

Lai, C. K., Meffre, S., Crawford, A. J., Zaw, K., Xue, C. D., and Halpin, J. A., 2014, The Western Ailaoshan Volcanic Belts and their SE Asia connection: A new tectonic model for the Eastern Indochina Block: Gondwana Research, v. 26, no. 1, p. 52-74.

Large, R. R., Meffre, S., Burnett, R., Guy, B., Bull, S., Gilbert, S., Goemann, K., and Danyushevsky, L., 2013, Evidence for an intrabasinal source and multiple concentration processes in the formation of the carbon leader reef, Witwatersrand Supergroup, South Africa: Economic Geology, v. 108, no. 6, p. 1215-1241.

Meffre, S., Large, R. R., Scott, R., Woodhead, J., Chang, Z., Gilbert, S. E., Danyushevsky, L. V., Maslennikov, V., and Hergt, J. M., 2008, Age and pyrite Pb-isotopic composition of the giant Sukhoi Log sediment-hosted gold deposit, Russia: Geochimica et Cosmochimica Acta, v. 72, no. 9, p. 2377-2391.

Müller, W., Shelley, M., Miller, P. & Broude, S. 2009. Initial performance metrics of a new custom-designed ArF excimer LA-ICPMS system coupled to a two-volume laser-ablation cell. Journal of Analytical Atomic Spectrometry, 24, 209-214.

Woodhead, J., Hergt, J., Meffre, S., Large, R. R., Danyushevsky, L., and Gilbert, S., 2009, In situ Pb-isotope analysis of pyrite by laser ablation (multi-collector and quadrupole) ICPMS: Chemical Geology, v. 262, no. 3-4, p. 380-390.

Wohlgemuth-Ueberwasser, C. C., Tegner, C., and Pease, V., 2017, LA-Q-ICP-MS apatite U/Pb geochronology using common Pb in plagioclase: Examples from layered mafic intrusions: American Mineralogist, v. 102, no. 3, p. 571-579.

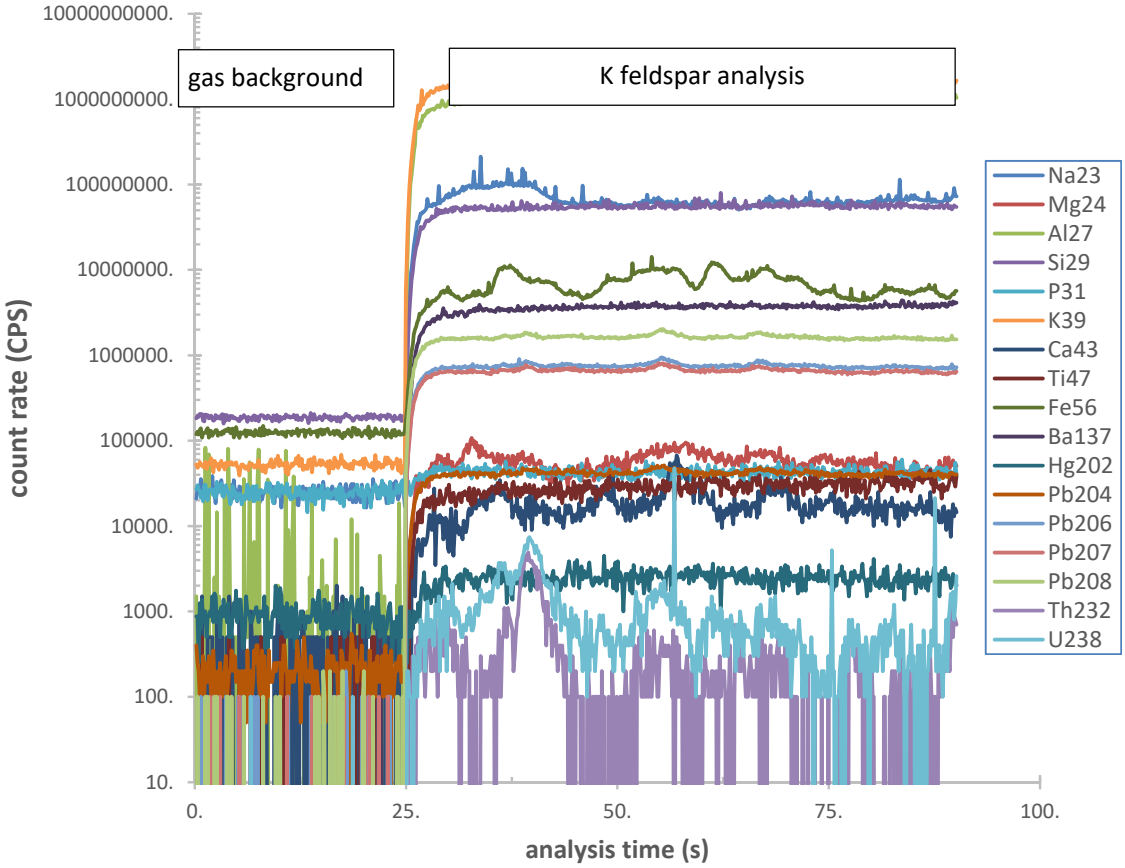

Appendix DR1 Figure 1. Typical analysis of K feldspar (FE15B0264 KC18-2-24) from sediments offshore Mirny Station. Pulse to analogue transition occurs as 1000000 cps.

Appendix 1 Table 1: Analytical parameters (after Cherry et al. 2018)

Laboratory and Sample Preparation	
Laboratory name	Earth Sciences/CODES, University of Tasmania
Sample type/mineral	In-situ, plagioclase and K-feldspar
Sample preparation	Conventional 1-inch rock mounts, 0.3 micron diamond polish. Cleaned in DI H_2O. Degassed in vacuum.
Laser ablation system	
Make, Model and type	Coherent COMPex Pro 110, RESOlution/Laurin Technic S155
Ablation cell and volume	Two volume laser cell with a volume 8.8 cm^3 small 2nd volume fixed cup
Laser wavelength (nm)	193 nm
Pulse width (ns)	ca. 20 ns
Fluence (J cm^{-2})	ca. 3.5 J/cm^2
Repetition rate (Hz)	10 Hz
Ablation duration (s)	90 seconds
Spot diameter (mm)	105-110µm feldspar and BCR-2G, 74 µm GSD-1G, 43µm NIST610
Sampling mode	line moving at 5 µm s^{-1}
Carrier gas	100% He in the cell set to 0.35 l/min, Ar carrier gas combined in 2nd volume of laser cell and was set to 1.05 l/min.
ICP-MS Instrument	
Make, Model and type	Agilent 7900 quadrupole ICPMS
Sample introduction	Ablation aerosol mixed with Ar and sent into ICP-MS
RF power (W)	1350 W
Detection system	Electron multiplier with Pb and U in pulse counting mode
Masses measured	Na23 Mg24 Al27 Si29 P31 K39 Ca43 Ti47 Fe56 Ba137 Hg202 Pb204 Pb206 Pb207 Pb208 Th232 U238
Integration time per peak/dwell times (ms)	5ms for masses from Na to Ba, 10ms for masses from Hg to U
Total integration time per output data point (s)	180 ms
IC Dead time (ns)	37

Data Processing	
Gas blank	25 s on-peak
Calibration strategy	NIST610 primary standard; analysed every hour
Reference Material info	http://georem.mpch-mainz.gwdg.de
Uncertainty level and propagation	Ratios for individual spots are at 1 sigma with final compilation and weighted averages on standards at 95% confidence levels. Uncertainty propagation is by quadratic addition of components of random uncertainty from unknowns, reference material, uncertainty in drift corrections.
Quality control / Validation	BCR-2G and GSD-1G check standards

Appendix DR2: Detailed assessment of sediment provenance

Prydz Channel Fan, Prydz Bay

ODP Site 1167 is located within the central part of the Prydz Channel Fan with hole 1167A sited at 66.40°S 72.28°E in a water depth of 1640 m on the upper slope and drilled to 447.5 metres below seafloor (O'Brien et al., 2001; Cooper and O'Brien, 2004). The available chronostratigraphy indicates that the sampled gravel and sand intervals (Fig. DR1) represent deposition during the early Pleistocene (> 1.13 Ma; sample 1167A-37 @322.8-326.37m, sample 1167A-39 @341.85-343.8m) and mid- to late Pleistocene (<1.13 Ma to 780 ka; sample 1167A-19 @150.55-155.52m, sample 1167A-22 @179.76-180.68m) (O'Brien et al., 2007). These coarse intervals are contained within Unit II (5.17 – 447.5 mbsf) debris flows, deposited within the grounding zone at the continental shelf edge. During this time, ice drainage into Prydz Bay included radial flow into the southern end of the Lambert Graben as well as NW-directed from the Ingrid Christensen Coast to the east (O'Brien et al., 2007).

There is a significant change in sediment composition at ~217 mbsf that is interpreted to reflect a shift in provenance related to depth of erosion and ice sheet volume (O'Brien et al., 2007). Below 217 mbsf reported pebble (lonestone) assemblages are dominated by sedimentary clasts, whereas above 217 mbsf there is a dominance of crystalline basement lithologies such as granite and gneiss. This change is replicated in clay mineralogy and other properties that provide evidence for a high proportion of recycled sedimentary material below 217 mbsf. However, available detrital zircon spectra are very similar in 1167A (Veevers et al., 2008a), as well as in Lambert Graben Permian-Triassic sedimentary rocks (Veevers and Saeed, 2008; Veevers et al., 2008b) suggesting recycling through Paleozoic-Mesozoic strata, and/or continued crystalline basement-derived detritus input throughout this period.

Given the Pleistocene paleo-ice flow directions, the grounding zone location, and the provenance interpretations in 1167A as outlined above, we interpret that the source of detrital feldspar grains from 1167A analysed in this study lies within the Amery-Lambert system. Despite the previously interpreted provenance change between the early and mid-late Pleistocene as outlined above, we find overlap in feldspar Pb-isotope ratios from samples above and below 217 mbsf (Fig. DR3), which could be explained in at least two ways: (1) recycling of detrital feldspar from crystalline basement through Lambert Graben sedimentary strata, or (2) continued erosion of at least some crystalline basement rocks surrounding the Lambert Graben throughout the sampled time interval. We would normally expect feldspar detritus to be first cycle, derived directly from volcanic products or crystalline basement rocks (e.g., Gwiazda et al., 1996; Tyrrell et al., 2007; Tyrrell et al., 2012). However, the dominance of mechanical weathering during glacial erosion could mean that survival of second cycle detrital feldspar (recycled through Lambert Graben sedimentary strata) is possible. While we cannot conclusively demonstrate which scenario is more likely with the current dataset, the detrital feldspar grains we analysed are angular to sub-angular suggesting limited transport and are therefore consistent with a first cycle derivation. Regardless, the overlap of Pb-isotope signatures from the detrital feldspar from 1167A and the exposed basement rocks in the immediate region, suggests that feldspar grains are an excellent proxy for the isotopic character of onshore geology.

Davis Sea, near Mirny Station

The available multibeam data from the R/V Nathaniel B. Palmer cruise 1 2001 (Leventer, 2013) shows that sampled karsten cores KC-18 and KC-22 and Grab-19 (Figs. DR1, DR2) were obtained in depressions on the shelf deep (Post et al., 2014) that resemble over-deepened troughs (Fig. DR4 inset (a)). Fine-scale ENE- to NE-trending lineations within the eastern trough are here interpreted as having formed due to wet-based glacial flow from the SW to NE, likely during the Last Glacial Maximum when the ice

edge extended some ~200 km further towards the shelf edge (Livingstone et al., 2012). The sampled troughs in the Davis Sea lack thick drift accumulations seen elsewhere along the margin, due to the bordering Shackleton Ice Shelf to the east (Leventer et al., 2001). The thin sediments sampled by karsten cores KC-18 and KC-22 are undated, but presumably represent dominantly hemipelagic deposition on the shelf during the Holocene after ice sheet retreat. The pebbles from Grab-19 were presumably also deposited during the Holocene to recent times.

We expect the provenance of the feldspar, zircon and monazite grains analysed here to be derived from coastal or near-coastal bedrock adjacent to the sampled locations, predominantly from the Wilhelm II Coast drainage basin (Mouginot et al., 2017), because: (1) we observe consistent detrital signature between sample locations and down core (Fig. DR3) suggesting provenance has not changed significantly over the sampled time interval, (2) the Shackleton Ice Shelf to the east is a barrier to far-travelled detritus, restricting drift deposits and the path of large icebergs (Fig. DR4) and (3) present-day surface and bottom current velocities measured in the region are <16 cm/s (Bindoff et al., 2000), which is not fast enough to move sand (>63 micron)-sized particles as analysed here (e.g., McCave et al., 2017). We also interpret the analysed detrital feldspar grains to have been derived directly from crystalline basement because they are relatively unaltered and angular to sub-angular in shape (Fig. 2B, inset). Small outlet glaciers, including the fast flowing Helen Glacier and streaming ice on the western side of the Shackleton Ice Shelf, likely provide terrigenous material to the shelf, possibly via proximal ice rafting (Fig. DR4 inset (b)), consistent with modelled areal scour erosion in this region (Jamieson et al., 2010; Jamieson et al., 2014).

References

Amante, C., and Eakins, B. W., 2009, ETOPO1 1 Arc-Minute Global Relief Model: Procedures, Data Sources and Analysis: NOAA Technical Memorandum NESDIS NGDC-24. National Geophysical Data Center, NOAA, http://dx.doi.org/10.7289/V5C8276M [Accessed September 2012].

Bindoff, N. L., Rosenberg, M. A., and Warner, M. J., 2000, On the circulation and water masses over the Antarctic continental slope and rise between 80 and 150°E: Deep Sea Research Part II: Topical Studies in Oceanography, v. 47, no. 12, p. 2299-2326.

Budge, J. S., and Long, D. G., 2018, A Comprehensive Database for Antarctic Iceberg Tracking Using Scatterometer Data: IEEE Journal of Selected Topics in Applied Earth Observations and Remote Sensing, v. 11, no. 2, p. 434-442.

Burton-Johnson, A., Black, M., Fretwell, P. T., and Kaluza-Gilbert, J., 2016, A fully automated methodology for differentiating rock from snow, clouds and sea in Antarctica from Landsat imagery: A new rock outcrop map and area estimation for the entire Antarctic continent: The Cryosphere Discussions, v. 2016, p. 1-16.

Cooper, A. K., and O'Brien, P. E., 2004, Leg 188 synthesis: transitions in the glacial history of the Prydz Bay region, East Antarctica, from ODP drilling, in Cooper, A. K., O'Brien, P. E., and Richter, C., eds., Proceedings of the Ocean Drilling Program, Scientific Results, 188, Volume 188, Ocean Drilling Program College Station, TX, p. 1-42.

Fretwell, P., Pritchard, H. D., Vaughan, D. G., Bamber, J. L., Barrand, N. E., Bell, R., Bianchi, C., Bingham, R. G., Blankenship, D. D., Casassa, G., Catania, G., Callens, D., Conway, H., Cook, A. J., Corr, H. F. J., Damaske, D., Damm, V., Ferraccioli, F., Forsberg, R., Fujita, S., Gim, Y., Gogineni, P., Griggs, J. A., Hindmarsh, R. C. A., Holmlund, P., Holt, J. W., Jacobel, R. W., Jenkins, A., Jokat, W., Jordan, T., King, E. C., Kohler, J., Krabill, W., Riger-Kusk, M., Langley, K. A., Leitchenkov, G., Leuschen, C., Luyendyk, B. P., Matsuoka, K., Mouginot, J., Nitsche, F. O., Nogi, Y., Nost, O. A., Popov, S. V., Rignot, E., Rippin, D. M., Rivera, A., Roberts, J., Ross, N., Siegert, M. J., Smith, A. M., Steinhage, D., Studinger, M., Sun, B., Tinto, B. K., Welch, B. C., Wilson, D., Young, D. A., Xiangbin, C., and Zirizzotti, A., 2013, Bedmap2: improved ice bed, surface and thickness datasets for Antarctica: The Cryosphere, v. 7, no. 1, p. 375-393.

Gwiazda, R. H., Hemming, S. R., and Broecker, W. S., 1996, Tracking the sources of icebergs with lead isotopes: The provenance of ice-rafted debris in Heinrich layer 2: Paleoceanography, v. 11, no. 1, p. 77-93.

Jamieson, S. S. R., Stokes, C. R., Ross, N., Rippin, D. M., Bingham, R. G., Wilson, D. S., Margold, M., and Bentley, M. J., 2014, The glacial geomorphology of the Antarctic ice sheet bed: Antarctic Science, v. 26, no. 6, p. 724-741.

Jamieson, S. S. R., Sugden, D. E., and Hulton, N. R. J., 2010, The evolution of the subglacial landscape of Antarctica: Earth and Planetary Science Letters, v. 293, no. 1–2, p. 1-27.

Leventer, A., 2013, Processed Multibeam Sonar Data (version 2) from the Southern Indian Ocean acquired during Nathaniel B. Palmer expedition NBP0101 (2001), https://doi.org/10.1594/IEDA/100399 [Accessed May 2018].
Leventer, A., Domack, E., Dunbar, G., McClennen, C., Brachfeld, S., Manley, P., and Pilskin, C., 2001, Sediment description for R/V Nathaniel B. Palmer Cruise 1, 2001.

Livingstone, S. J., Ó Cofaigh, C., Stokes, C. R., Hillenbrand, C.-D., Vieli, A., and Jamieson, S. S. R., 2012, Antarctic palaeo-ice streams: Earth-Science Reviews, v. 111, no. 1, p. 90-128.

McCave, I. N., Thornalley, D. J. R., and Hall, I. R., 2017, Relation of sortable silt grain-size to deep-sea current speeds: Calibration of the 'Mud Current Meter': Deep Sea Research Part I: Oceanographic Research Papers, v. 127, p. 1-12.

Mouginot, J., Scheuchl, B., and Rignot, E., 2017, MEaSUREs Antarctic Boundaries for IPY 2007-2009 from Satellite Radar, Version 2: Boulder, Colorado USA. NASA National Snow and Ice Data Center Distributed Active Archive Center, http://dx.doi.org/10.5067/AXE4121732AD [Accessed 24 April 2017].

O'Brien, P., Cooper, A., Richter, C., and al., e., 2001, Proceedings of the Ocean Drilling Program, Initial Reports. Vol. 188.: Texas A & M University Ocean Drilling Program.

O'Brien, P., Goodwin, I., Forsberg, C.-F., Cooper, A., and Whitehead, J., 2007, Late Neogene ice drainage changes in Prydz Bay, East Antarctica and the interaction of Antarctic ice sheet evolution and climate: Palaeogeography, Palaeoclimatology, Palaeoecology, v. 245, no. 3-4, p. 390-410.

Post, A., Meijers, A., Fraser, A., Meiners, K., Ayers, J., Bindoff, N., Griffiths, H., Van de Putte, A., O'Brien, P., Swadling, K., and Raymond, B., 2014, Chapter 14. Environmental Setting, in de Broyer, C., Koubbi, P., Griffiths, H., Raymond, B., and d'Udekem d'Acoz, C., eds., Biogeographic Atlas of the Southern Ocean: Scientific Committee on Antarctic Research, Cambridge UK, p. 46-64.

Rignot, E., Mouginot, J., and Scheuchl, B., 2017, MEaSUREs InSAR-Based Antarctica Ice Velocity Map, Version 2: Boulder, Colorado USA. NASA National Snow and Ice Data Center Distributed Active Archive Center, http://dx.doi.org/10.5067/D7GK8F5J8M8R [Accessed 24 April 2017].

Tyrrell, S., Haughton, P. D., Daly, J. S., and Shannon, P. M., 2012, The Pb isotopic composition of detrital K-feldspar: A tool for constraining provenance, sedimentary processes and paleodrainage: Quantitative Mineralogy and Microanalysis of Sediments and Sedimentary Rocks. Mineralogical Association of Canada, Short Course Series, v. 42, p. 203-217.

Tyrrell, S., Haughton, P. D. W., and Daly, J. S., 2007, Drainage reorganization during breakup of Pangea revealed by in-situ Pb isotopic analysis of detrital K-feldspar: Geology, v. 35, no. 11, p. 971-974.

Veevers, J. J., and Saeed, A., 2008, Gamburtsev Subglacial Mountains provenance of Permian-Triassic sandstones in the Prince Charles Mountains and offshore Prydz Bay: Integrated U-Pb and TDM ages and host-rock affinity from detrital zircons: Gondwana Research, v. 14, no. 3, p. 316-342.

Veevers, J. J., Saeed, A., and O'Brien, P. E., 2008a, Provenance of the Gamburtsev Subglacial Mountains from U-Pb and Hf analysis of detrital zircons in Cretaceous to Quaternary sediments in Prydz Bay and beneath the Amery Ice Shelf: Sedimentary Geology, v. 211, no. 1-2, p. 12-32.

Veevers, J. J., Saeed, A., Pearson, N., Belousova, E., and Kinny, P. D., 2008b, Zircons and clay from morainal Permian siltstone at Mt Rymill (73¬∞S, 66¬∞E), Prince Charles Mountains, Antarctica, reflect the ancestral Gamburtsev Subglacial Mountains-Vostok Subglacial Highlands complex: Gondwana Research, v. 14, no. 3, p. 343-354.

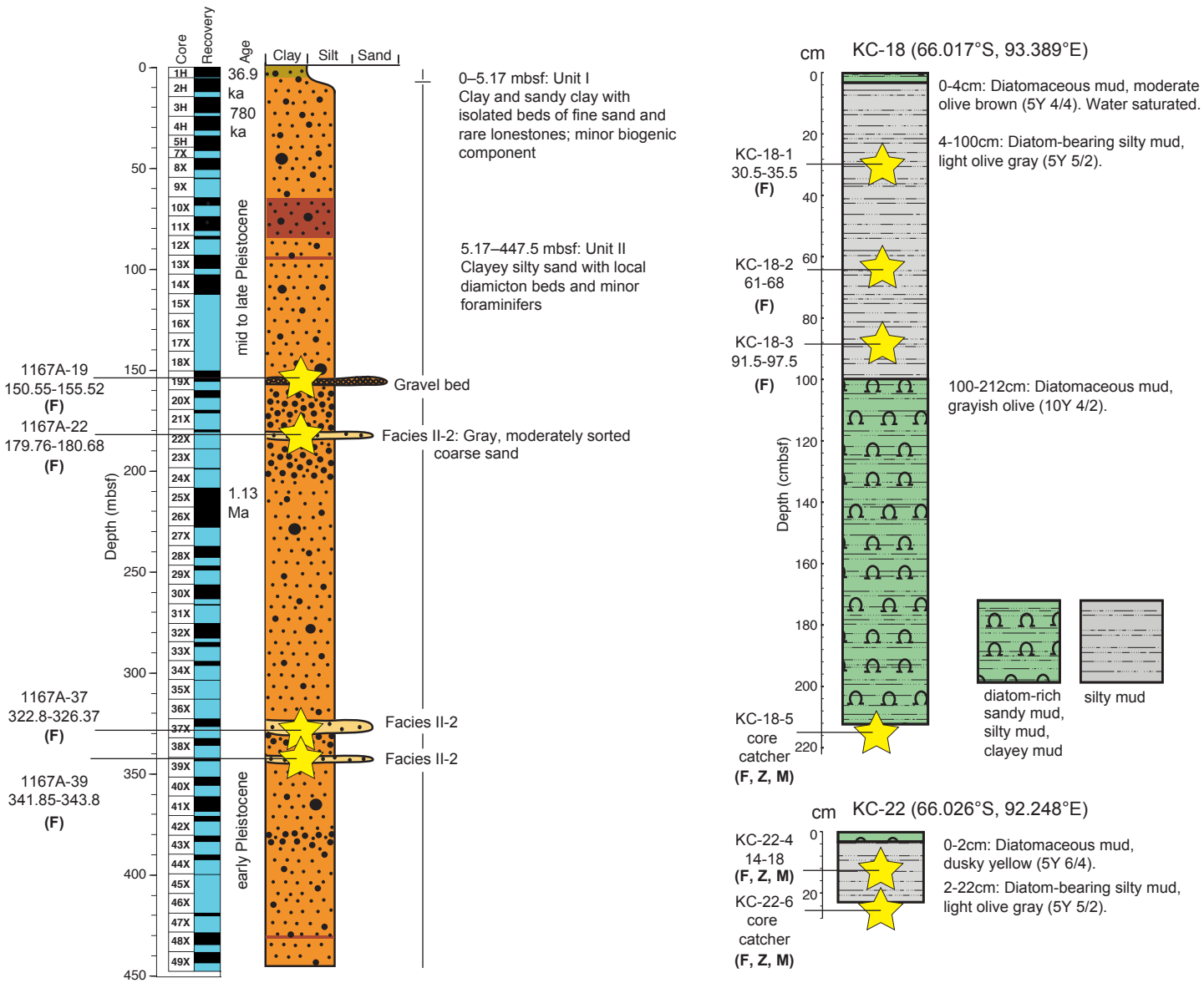

Figure DR1. (a) Simplified core log from ODP 1167A showing the sample locations used in this study. Adapted from Veevers et al. (2008), Cooper & O'Brien (2004) and O'Brien et al. (2007). All samples were provided by John Veevers and represent a subsample of the original sample volume from Veevers et al. (2008). (b) Simplified core logs from NBP01-01 showing the sample locations and numbering system used in this study. Sampled core volumes were 40 cc, and core catcher samples were 150g (wet weight). All samples were provided by the Antarctic Research Facility, Florida State University. Analysed detrital minerals: F= feldspar, Z=zircon, M=monazite.

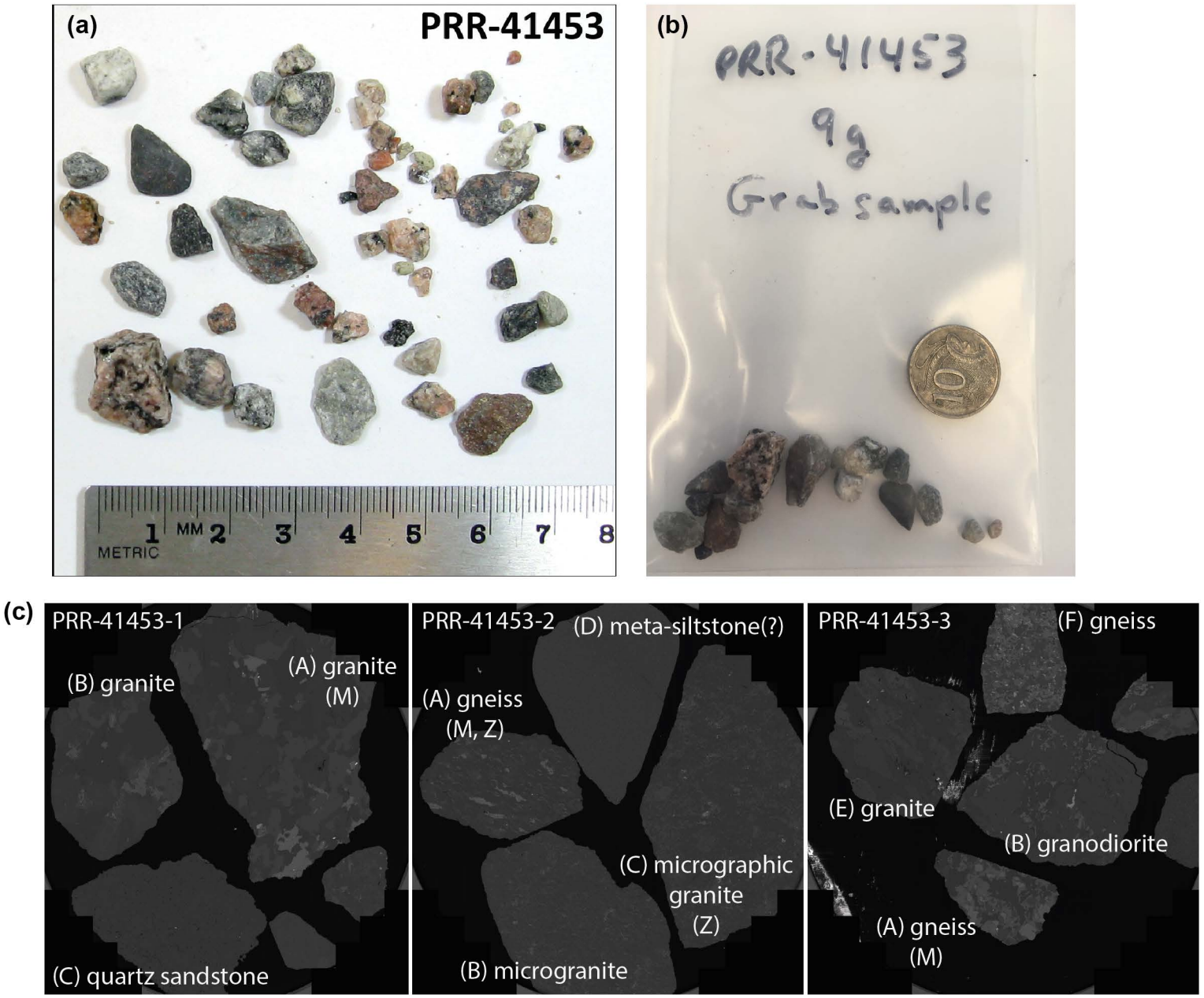

Figure DR2. (a) Pebbles from NPB01-01 Grab-19 (PRR-41453) as photographed by the Polar Rock Repository, Byrd Polar & Climate Research Center, Ohio State University. (b) Sub-sampled pebbles from the PRR-41453 collection, at a total weight of 9 g. (c) Back scatter electron images of pebbles. Those analysed for U-Pb zircon and/or monazite are highlighted: Z=zircon, M=monazite.

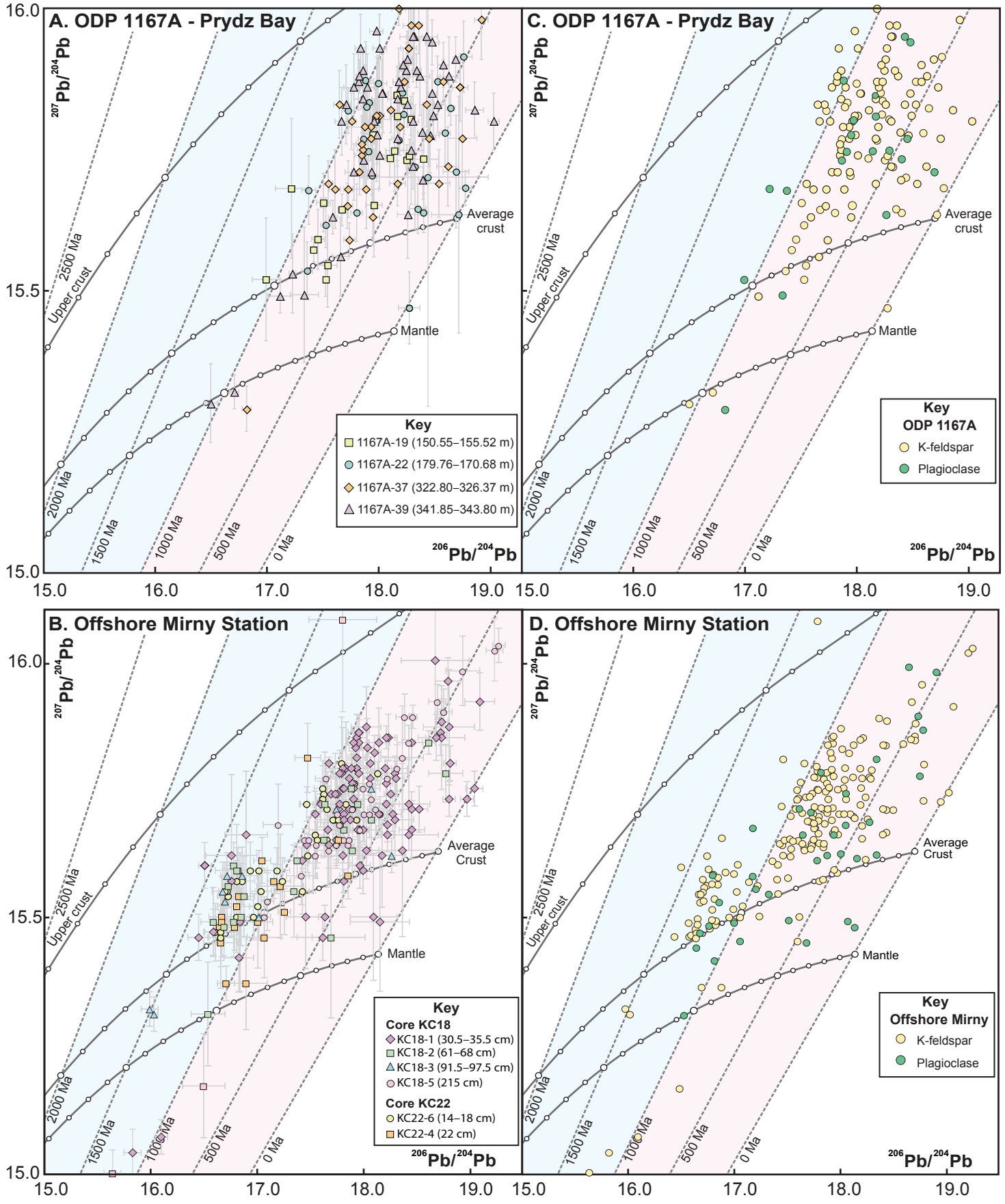

Figure DR3: Detrital feldspar Pb-isotope data plotted by sample depth (A and B) and feldspar type (C and D). Error bars are 2σ. Isochrons are shown as dashed grey lines labelled in Ma; blue and pink shading highlight typical range of feldspar Pb-isotope compositions from Australo-Antarctic and Indo-Antarctic basement, respectively. Solid grey curved lines show time-integrated Pb-isotope evolution of different sources (Stacey and Kramers, 1975), marked in 100 Ma increments. There is no systematic correlation between Pb-isotope composition and the depth of samples in the sediment cores (A and B) or feldspar type (C and D). Importantly, both the Australo-Antarctic and the Indo-Antarctic feldspar Pb-isotope signatures in the sediments offshore from Mirny Station are present in all sampled intervals of both cores (B) and are recorded by both K-feldpsar and plagioclase (D).

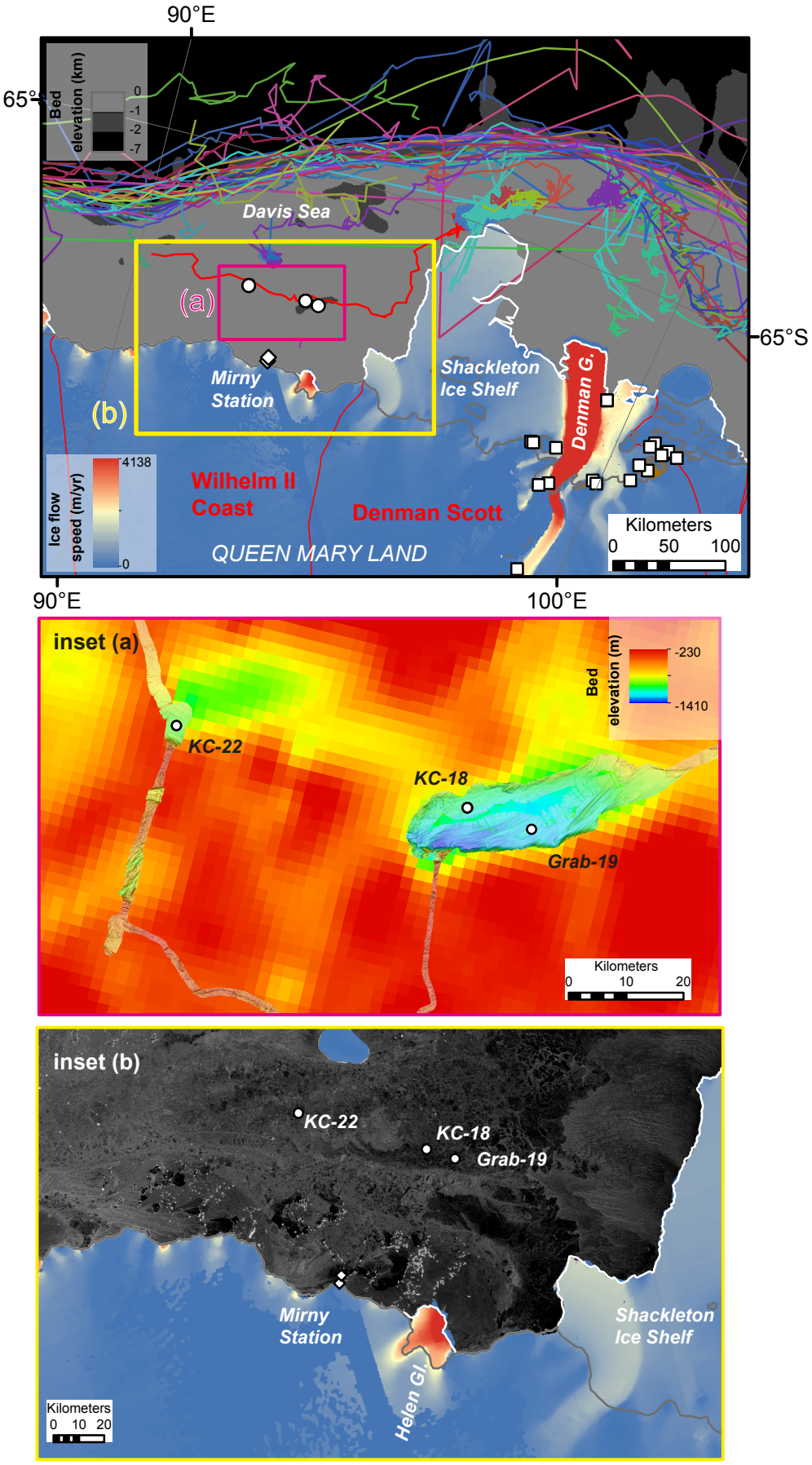

Figure DR4. Glacial and oceanographic context for samples from the Mirny region, Davis Sea. Large (>5km 2) icebergs dominantly drift from east to west along the continental shelf within the Antarctic Shelf Current (iceberg tracks 1992-2007; Budge and Long, 2018; http://www.scp.byu.edu/iceberg/). Only one large iceberg has transited across the Mirny region (red line offshore) over a period of ~25 days between longitude 094°E and 092°E, and therefore icebergs carrying detritus derived from the east are unlikely to contribute to sediment deposition along the shelf deep adjacent to Mirny. Background datasets include Bedmap2 DEM (Fretwell et al., 2013), Landsat-derived rock outcrop (Burton-Johnson et al., 2016), MEaSUREs 450m resolution ice flow velocity (Rignot et al., 2011) and MEaSUREs-derived Antarctic boundaries including ice drainage basins (red text and red line boundaries), coastline and grounding line (Mouginot et al., 2017). Sample locations shown with symbology as per Fig. 1.

Inset (a). Bathymetric detail in the Davis Sea adjacent to Mirny Station. High resolution multibeam from NBP01-01 (Leventer, 2013) with a hillshade is overlain on ETOPO1 (Amante and Eakins, 2009) at the same depth scale. The sample locations intersect over-deepened troughs. Note the fine-scale ENE- to NE-trending lineations in the eastern trough, interpreted as having formed due to wet-based glacial flow from the SW to NE, possibly during the Last Glacial Maximum.

Inset (b). Sentinel 1b SAR Extended Wide Swath image taken on 3/5/18 showing most icebergs in the Mirny region are relatively small (mostly <600-1000m across) and calve directly from small outlet glaciers. Image data courtesy European Space Agency, image provided by PolarView: https://www.polarview.aq/antarctic. MEaSUREs 450m resolution ice flow velocity shown on the continent and ice shelves (Rignot et al., 2011).